

# Journal of Biomedical Optics

BiomedicalOptics.SPIEDigitalLibrary.org

## Review of near-infrared methods for wound assessment

Michael G. Sowa  
Wen-Chuan Kuo  
Alex C-T. Ko  
David G. Armstrong

# Review of near-infrared methods for wound assessment

Michael G. Sowa,<sup>a,\*</sup> Wen-Chuan Kuo,<sup>b</sup> Alex C-T. Ko,<sup>a</sup> and David G. Armstrong<sup>c</sup>

<sup>a</sup>National Research Council Canada, Medical Devices Portfolio, 435 Ellice Avenue, Winnipeg, Manitoba R3B 1Y6, Canada

<sup>b</sup>National Yang-Ming University, Institute of Biophotonics, No.155, Sec.2, Linong Street, Taipei 112, Taiwan

<sup>c</sup>University of Arizona College of Medicine, Vascular/Endovascular, P.O. Box 245072, Tucson, Arizona 85724-5072, United States

**Abstract.** Wound management is a challenging and costly problem that is growing in importance as people are living longer. Instrumental methods are increasingly being relied upon to provide objective measures of wound assessment to help guide management. Technologies that employ near-infrared (NIR) light form a prominent contingent among the existing and emerging technologies. We review some of these technologies. Some are already established, such as indocyanine green fluorescence angiography, while we also speculate on others that have the potential to be clinically relevant to wound monitoring and assessment. These various NIR-based technologies address clinical wound management needs along the entire healing trajectory of a wound. © 2016 Society of Photo-Optical Instrumentation Engineers (SPIE) [DOI: [10.1117/1.JBO.21.9.091304](https://doi.org/10.1117/1.JBO.21.9.091304)]

Keywords: fluorescence angiography; optical coherence tomography; photoplethysmography; near-infrared imaging; nonlinear optical imaging; inflammation; proliferation; remodeling.

Paper 160014SSVR received Jan. 8, 2016; accepted for publication Mar. 4, 2016; published online Apr. 18, 2016.

## 1 Introduction

The body has a remarkable ability to heal itself. Despite a broad etiology ranging from acute trauma to complications arising from diabetes, atherosclerosis, tissue compression, and malignancy, healing soft tissue wounds share a common trajectory described as a series of overlapping phases associated with hemostasis, inflammation, proliferation, and remodeling. Figure 1 is a sequence of illustrations that capture some of the key features of the phases of wound healing. Underlying these phases is a complex choreography of molecular and cellular processes. Healing is impaired when this choreography is disrupted. Wound management attempts to steer wounds along a healing trajectory to optimize functional and esthetic outcomes. Monitoring healing progression plays a key role in effective wound management. Clinical monitoring comprised of visible inspection and physical examination remains the cornerstone of wound assessment. However, instrumental methods play an increasingly important role. Many of these clinically adopted and emerging technologies are photonics based instruments that employ near-infrared (NIR) light. The optical properties of soft tissue lend themselves to interrogation by NIR radiation. NIR light is weakly absorbed but highly scattered by tissue, thereby enabling this light to penetrate tissue more deeply than ultraviolet, visible, and infrared radiation.<sup>1</sup> This deeper penetration is one of the factors why NIR light is employed for the assessment of wounds. This manuscript will review some of the NIR based methods that are used for wound assessment.

## 2 Clinical and Social Challenges

Our species' population is aging. This has occurred at a logarithmic rate over the past 100 years because of advances in

public health, anti-infectives, nutrition, and other aspects of health delivery. The past decade marked the first in the history of humanity where more people died of noninfectious diseases (noncommunicable diseases or NCDs) than from all the plagues in the world combined.<sup>2</sup> This dramatic change in our makeup will necessarily focus our attention from diseases of infection to diseases of decay.<sup>2,3</sup>

One of the first biological matrices to decay in many older people is their integument. Treating these chronic wounds is surprisingly common, complex, and costly. In fact, the cost for treating those with diabetes alone exceeds the direct costs of the five most expensive cancers and is associated with comparable if not greater mortality.<sup>4-6</sup> While it would stand to reason that focus on this problem should be commensurate with its public health impact, this has not been the case. In fact, measuring and managing tissue loss constitutes a major unmet need in medicine, surgery, and policy.<sup>7,8</sup>

## 3 Brief Description of Wound Healing

The healing process begins immediately following the injury.<sup>9-11</sup> When tissue injury disrupts blood vessels and causes bleeding, potent vasoconstrictors are released at the site of the injury and the process of blood coagulation and clotting begins. This early response after an acute injury is aimed at limiting blood loss and preserving the vascular system and hemostasis. However, as structural elements of the clot form from collagen, platelets, thrombin, and fibronectin, growth factors, and cytokines are released and trigger the cellular component of the inflammatory response. The release of proinflammatory mediators leads to rapid expression of adhesion proteins on the surface of endothelial cells of the vessel wall and other chemoattractants which begin to recruit and guide leukocytes to the region of the injury. Neutrophils arrive at the wound site soon after injury to deal with invading pathogens. Concurrently, lymph drainage is reduced and blood is moved to the extravascular space. As

\*Address all correspondence to: Michael G. Sowa, E-mail: [mike.sowa@nrc-cnrc.gc.ca](mailto:mike.sowa@nrc-cnrc.gc.ca)

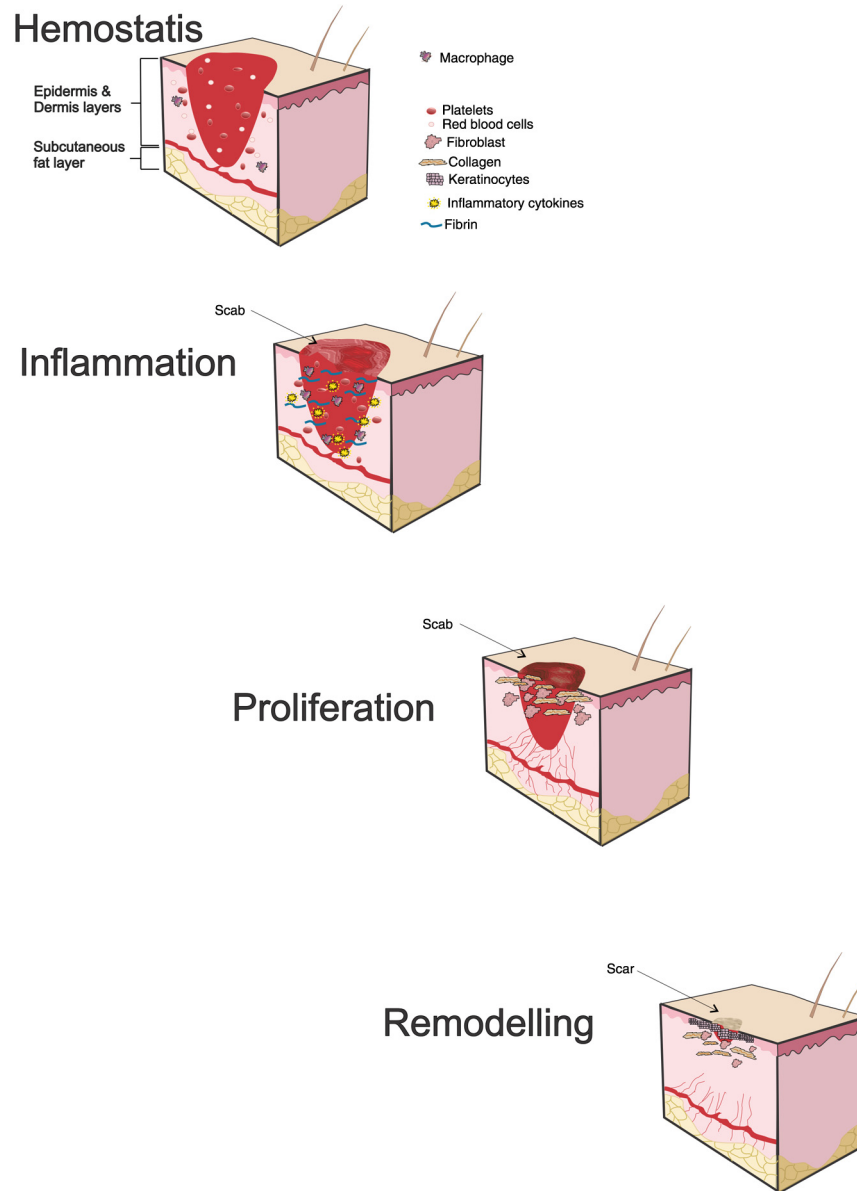


**Fig. 1** Illustration of the phases of wound healing. Healing of soft tissue is often portrayed in four phases that overlap. Phase 1, hemostasis, is associated with vasoconstriction and coagulation. In phase 2, inflammation, the innate immune system is activated and molecular/cellular repair machinery is assembled. The proliferative phase is characterized by extensive angiogenesis and extracellular matrix deposition. In the remodeling phase the neovasculature is revised and matured, collagen networks are strengthened, and scar formation is completed.

inflammatory mediators accumulate, blood vessels surrounding the wound are triggered to vasodilate to enable more cells to reach the wound. Clinically, this acute inflammatory phase is characterized by tissue redness, swelling, and the sensation of heat. Neutrophil activity at the wound site gradually gives way to monocyte-derived macrophages. Monocytes from the surrounding tissue and circulating blood begin to migrate to the wound site and gradually transform into macrophages as they debride the wound of nonviable tissue.<sup>12</sup> Proinflammatory macrophages, often described as the M1 functional phenotype, drive the early stages of the inflammatory phase, which is largely centered around host defense. The bacteria, cellular, and tissue phagocytosis performed by the macrophages and the subsequent release of chemotactic and angiogenic factors leads to

macrophages of an M2 functional phenotype and a transition to the proliferative phase of healing.<sup>12-15</sup> The proliferative phase is dominated by cellular processes leading to re-establishing the blood supply to the wound site through angiogenesis, providing wound coverage through re-epithelialization and rebuilding the basement membrane that connects the epidermis to the underlying dermis. Re-establishing the blood supply to the healing wound through angiogenesis is paramount given the high energetic demands during proliferation. Hypoxia and macrophages play an important role in directing angiogenesis as hypoxic macrophages release angiogenic factors.<sup>12,13</sup> Thus, new vessels begin to form from the vascularized periphery of the wound toward the avascular hypoxic center of the wound. The high metabolic demand associated with the

proliferative phase results in a vascular density well beyond what is normally found in native tissue.<sup>16</sup> Much of newly established capillary system is reversed during the remodeling phase as cellular metabolic demand diminishes. Components of the extracellular matrix (ECM) play a role throughout the healing process, being involved in signal transduction, stimulating cellular adhesion, and migration and being a store of cytokines and growth factors. During the proliferative phase of healing the temporary structural matrix formed from fibrin and fibronectin is gradually replaced by a loose network of neovasculature and collagen which is extensively populated by fibroblasts, keratinocytes, and endothelial cells. This initial coverage of the wound bed is usually referred to as granulation tissue.<sup>17</sup> The classical view of healing during this period is that during the late stages of inflammation, fibroblast production in the surrounding tissue is stimulated, and then these cells begin to migrate to the wound site where they further proliferate as myofibroblasts. Current thought favors multiple origins of myofibroblasts.<sup>18</sup> Regardless of their origin, these cells combine the features of contractile smooth muscle cells and the ECM synthesis of fibroblasts. The granulation tissue laid down consists of a high proportion of type III collagen, elastin, proteoglycans, glycosaminoglycans, and noncollagenous proteins. The contractile forces exerted by myofibroblasts on the surrounding collagen lead to repeatedly stressed collagen, helping align the collagen and contributing to wound contraction.<sup>19</sup> Collagen provides a foundation for the extracellular matrix, imparting integrity and strength to the healed wound. The collagen III that was laid down during the proliferating phase is replaced by collagen I. The total collagen content in the wound increases, and it becomes more spatially organized and more cross-linked, leading to an increase in tensile strength. However, the subsequent scar which is the endpoint of mammalian cutaneous wound healing does not have the same structural strength as before the injury because the newly formed collagen I network is oriented in small parallel bundles as opposed to the basket-weave structure of native skin. As epithelial coverage of the wounds is complete, myofibroblasts disappear through apoptosis. Also, in the remodeling phase, apoptosis leads to a regression of much of the newly formed vascular network, resulting in reduced blood flow as a result of decreased metabolic activity at the site of the healed injury.

#### 4 Factors Affecting Wound Healing

Despite our growing understanding of the healing process, wounds remain a challenging clinical problem.<sup>20–24</sup> Complications leading to morbidity or mortality can arise at any phase along the healing trajectory, with the global social and economic impact of impaired wound healing being enormous. There are a large number of systemic and local factors that can influence healing. Systemic factors include age, stress, diabetes, obesity, alcohol consumption, smoking, and nutrition. Clinical guidance plays an important role in helping the patient manage these systemic risk factors, which in turn is an important part of wound management. While systemic factors are important, many are not easily influenced or actionable while some require the patient to commit to lifestyle changes. Most wound monitoring technologies assess one or more local factors that can direct clinical response.

Perhaps the key local factor determining wound outcome in addition to appropriate protection is adequate perfusion of the wound with oxygenated blood.<sup>25–29</sup> Wounds are generally ischemic-hypoxic. Mild ischemia-hypoxia is generally considered to

be angiogenic, and a number of compensatory systems enable tissue to cope under such conditions. However, moderate to severe ischemia-hypoxia provides an environment for anaerobic bacteria and leads to rapid tissue necrosis. The metabolically active wound site can be hypoxic with no detectable deficiency in blood supply. Similarly, microvascular perfusion and oxygen transport can be compromised with large vessel perfusion remaining intact. In addition to being vital for glucose metabolism to meet the energy demands of the wound site, oxygen is crucial for cell proliferation, bacteria defense, and angiogenesis as well as collagen cross-linking, which is essential for providing tensile strength to the healed wound. The surgeon has a number of surgical and nonsurgical approaches to re-establish or enhance perfusion and oxygenation to the wound. Given the importance of perfusion and oxygenation to wound outcome and that action can be taken if perfusion or oxygenation is considered inadequate, it is not surprising to find that most wound monitoring technologies provide some form of measure of perfusion or oxygenation. However, as pointed out above, measures of perfusion and oxygenation are not surrogates for each other. Perfusion provides a measure of supply while measures related to oxygen at the wound site are dependent on both supply and metabolic demand. Therefore, measuring both perfusion and oxygenation would seem to be advantageous in determining the balance between oxygen-nutrient delivery and metabolic demand.

Edema is another local factor that can impair healing. Extravasation of blood and fluids from the wound can build fluid pressure in the tissue surrounding the wound. Fluid pressures in the neighborhood of 32 mmHg cause closure of vessels in the capillary bed,<sup>30</sup> exacerbating ischemia-hypoxia of the wound. Edema is particularly evident in burn injuries where there can be massive transvascular flux of fluids and where fluid resuscitation strategies can further compound tissue edema.<sup>31</sup> Pressure and shear forces applied to the wound can also lead to direct deformational damage to the wound as well as capillary closure leading to cellular disruption and microvascular damage arising from ischemia-reperfusion injury.<sup>32</sup> Scarring and the eventual mechanical properties of the healed wound are influenced by the extrinsic mechanical forces that are applied to the wound during proliferation and remodeling.<sup>33,34</sup> When appropriately applied extrinsic mechanical forces can lead to enhanced healing and potentially less scarring. This appropriate manipulation of forces is one of the benefits potentially conveyed by vacuum-assisted wound healing devices.

Necrotic tissue and foreign bodies can prolong the inflammatory phase and lead to delayed and disrupted healing. They can also be entry points for bacteria to the wound site as well as providing a matrix for the formation of bacterial biofilms.<sup>35</sup> Wound debridement serves to eliminate this obstacle to wound healing.<sup>25</sup> Without the protective barrier that intact skin provides, wounds are highly prone to infection. This can arise through self-contamination, direct contact, or airborne dispersal of colonizing microorganisms. While the virulence of the organism and the immunological status of the patient play an important role in determining the fate of the wound, if the bacterial count exceeds  $10^5$  organisms/gram of tissue the wound will not heal.<sup>20</sup> Local wound infection is a serious impediment to healing, and prevention and abatement of wound infection are important objectives of wound management.

Delayed healing, often attributed to prolonged inflammation, extensive myofibroblast infiltration, and excessive collagen

production can lead to dermal fibrosis and pathological scar formation.<sup>36,37</sup> There is also evidence that extensive angiogenesis can be a source of abnormal scar formation in healing wounds.<sup>38</sup> In addition to being aesthetically displeasing, keloids and hypertrophic scars can be psychologically devastating, painful, and pruritic. Surgical, biomechanical, and pharmacological interventions are evolving to reduce scar formation,<sup>39</sup> and instrumental techniques to monitor treatment efficacy as well as detect and distinguish between ECM overproduction and aberrant collagen deposition could have practical utility in the effort to reduce keloid and hypertrophic scarring.

Two recent review articles outlined some of the technologies that can be used to monitor wound healing.<sup>40,41</sup> In this review, we focus on methods that use NIR radiation to assess one or more of the factors that affect healing and that have the potential to be important tools in the clinical management of wounds.

## 5 Near-Infrared Methods to Assess Wound Perfusion

Poor perfusion or ischemia is often complicit in delayed wound healing. Given the importance of good arterial supply and venous drainage of blood to and from wounds, various NIR-based techniques have been developed to measure local blood flow or perfusion. For an extensive review of blood flow imaging methods that is not restricted to NIR methods, the reader is referred to the article by Daly and Leahy.<sup>42</sup>

### 5.1 Indocyanine Green—Angiography

Angiographic flow tracer methods using dyes have a long history<sup>43,44</sup> and have re-emerged as an important method to visualize wound perfusion using indocyanine green (ICG) fluorescence imaging.<sup>45–48</sup> Angiographic methods employ a contrast agent and track its distribution and transit time in the vascular bed of interest in order to visualize the lumen of larger vessels, track the supply and transit of blood to the capillary bed, and image lymphatic vessels. In the vast majority of instances, this is done using an intravenously administered bolus dose of the contrast agent. The earliest applications made use of visible dyes such as fluorescein that could be followed by eye, without the need for any electronic cameras. However, NIR light absorbing and emitting agents enable visualization of deeper vascular networks compared with angiographic methods based on ultraviolet or visible light absorption and fluorescence. The workhorse dye for clinical angiographic measurements has been the NIR dye ICG. It is widely used in humans for a number of indications,<sup>45–60</sup> and there are specific ICG imaging products on the market for wound assessment and intraoperative assessment of perfusion.

ICG is a water-soluble tricyanobenzene (anhydro-3,3,3',3'-tetramethyl-1-1'-di-(4-sulfobutyl)-4,5,4',5'-dibenzoindotriazine hydroxide sodium salt) dye with both lipophilic and hydrophilic characteristics. The fluorescence excitation and emission characteristics of the dye show both a solvent and concentration dependence.<sup>61</sup> However, aqueous solutions of  $5 \mu\text{mol L}^{-1}$  or less show an excitation maximum around 790 nm with an emission maximum around 820 nm (see Fig. 2).

For clinical use, ICG is usually provided as a sterile lyophilized green powder containing no more than 5% sodium iodide to aid water solubility. It should be dissolved in sterile water as the dye tends to precipitate at high concentrations when mixed in physiological saline. Intravenous administration should be

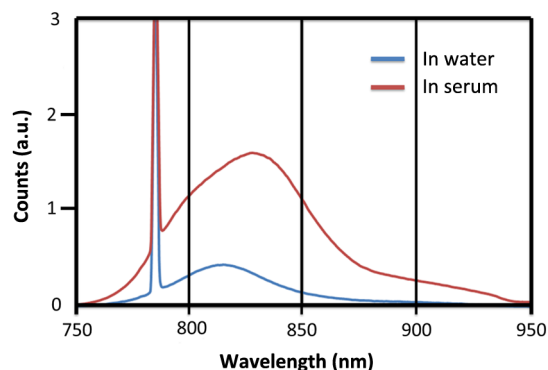


**Fig. 2** Fluorescence emission spectrum of ICG excited at 785 nm in both aqueous solution and serum at a weight volume of 0.075 mg/ml. A signal enhancement is observed in serum due to protein binding and improved fluorescence quantum yield. A broader and more red-shifted emission is observed in serum compared to water.

carried out within 10 h of preparation with minimal exposure of the dye solution to UV light as it is prone to photodegradation.<sup>62,63</sup> The use of the dye is contra-indicated in patients with iodine allergy, and it should also be avoided in uremic patients and in those with liver disease.<sup>62</sup> Its safety for pregnant women is not well studied.<sup>64</sup> Adverse reactions to ICG are rare, with pruritus and mild reactions such as nausea and vomiting occurring in about 0.15% of patients.<sup>65</sup> More severe reactions have been reported and some deaths have occurred during cardiac catheterization in conjunction with ICG administration. ICG extravasation is well-tolerated and resolves without complications. Following intravenous injection, ICG is rapidly bound to plasma proteins and is almost exclusively taken up from the plasma by the liver and excreted into the bile without metabolic alteration.<sup>66–68</sup> In healthy individuals, the rate of ICG disappearance from the vascular compartment is 18% to 24%/min with a half-life of 2 to 4 min; after 20 min, no more than 4% of the initial concentration of the dye should remain in the serum.<sup>63</sup> The fast clearance from the bloodstream makes repeated injections and perfusion measurements possible.

Together, its low level of toxicity, short vascular half-life and excretion, and rapid binding to serum proteins, which confine it to the vascular compartment during transit, make ICG a useful flow tracer for visualizing perfusion to the wound. Figure 3 shows an example of using ICG in-flow kinetics to distinguish areas of a pedicle skin flap with inadequate perfusion. The left panel shows fluorescence intensity measurements made with a video frame rate camera capturing the first-pass transit of the dye after administration of a bolus dose of ICG. Four distinct in-flow kinetic profiles were observed that correspond to different areas of the flap and native tissue. In this example, it is apparent that perfusion to the distal portion of the flap is compromised.

Sequential monitoring requires further administration of the dye with the frequency of monitoring being limited by the clearance of the dye. There is a nonspecific binding of ICG to the vascular endothelium. Eventually the build-up of vessel-bound ICG leads to a large enough fluorescence background to significantly reduce the contrast from the first-pass transit of the dye most recently injected. However, when the frequency of monitoring is low and the number of dye injections are few, these limitations do not come into play and the method is an

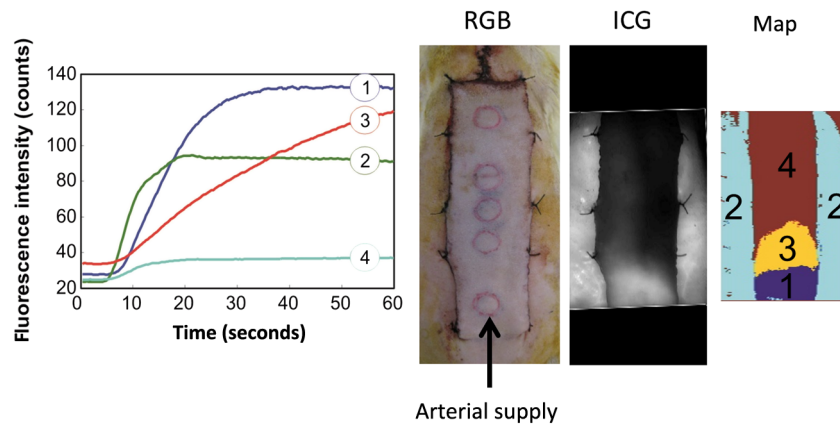


**Fig. 3** ICG angiography. The left panel shows the in-flow kinetics of the tracer into a pedicle skin flap, having four distinct time courses. The second panel shows a color digital picture of the flap, which has an isolated vascular supply at the proximal end of the flap. The third panel shows the integrated ICG fluorescence intensity. The distal end of the flap shows little ICG fluorescence, indicating low perfusion. The right panel shows the regions of the tissue that have the ICG inflow kinetics depicted in the first panel. These different perfusion kinetic traces arise in four distinct regions of the flap that are visualized in the right panels 1 to 4 of the figure. The base of the flap near the vascular supply (proximal end) and the native tissue show rapid in-flow kinetics (traces 1 and 2), the central portion of the flap shows slow but sustained in-flow (trace 3), while the distal portion of the flap shows only modest in-flow of the tracer (trace 4).

intuitively appealing means to visualize local tissue perfusion; see Fig. 4. Recent clinical experience suggests ICG angiography can play a role in documenting perfusion deficits in patients with peripheral arterial disease<sup>53</sup> and microvascular dysfunction in patients with diabetic neuropathy,<sup>54</sup> as well as providing a quantitative prognostic outcome assessment following revascularization procedures.<sup>55</sup>

## 5.2 Laser Speckle Contrast Imaging

The requirement to inject a dye represents a major shortcoming of ICG fluorescence angiography when positioning the technology as a routine wound monitoring device.<sup>69–73</sup> Noninvasive alternatives to visualize perfusion seem better suited to that role. One such class of methods exploits the variance of laser speckle imparted by flooding blood. Laser speckle is produced when a coherent source is incident on a nonspecular scattering target. The light scattering properties of the target can impart path length differences in the reflected coherent light reaching the detector element. When backscattered coherent light from

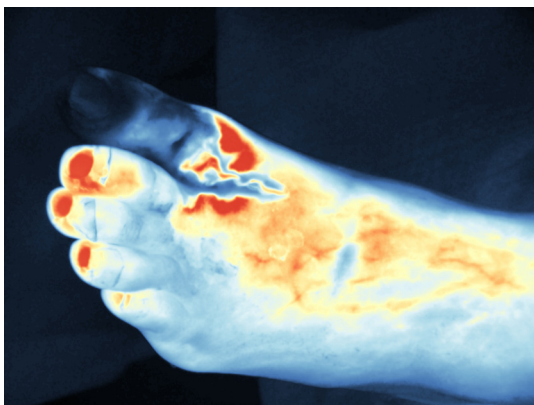


**Fig. 4** ICG near-infrared fluorescence angiography (using the LUNA system, Novadaq Technologies Inc.) of a problematic foot with an ischemic toe.

the illuminated target is measured, the intensity of the measured light is the resulting superposition of all the light waves reaching the detector element. When the target is imaged this interference gives rise to a grainy intensity (interference) pattern or speckle pattern. The coherence of the light and the properties of the scattering target dictate the speckle pattern. Moving scattering centers within the target causes the speckle pattern to fluctuate in time, whereas if the scattering centers are static the speckle pattern remains static. Time-integrated images of speckle patterns display sharp contrast between bright and dark speckles when the scattering target is not in motion and reduced contrast (or blurring) when the scattering centers within the target are in motion. Figure 5 shows two raw speckle patterns; one pattern has high contrast while the second is blurred due to the motion of scattering centers.

The speckle contrast of an image is usually given by the ratio of the standard deviation  $\sigma_s$  of the intensity,  $I$ , to the mean

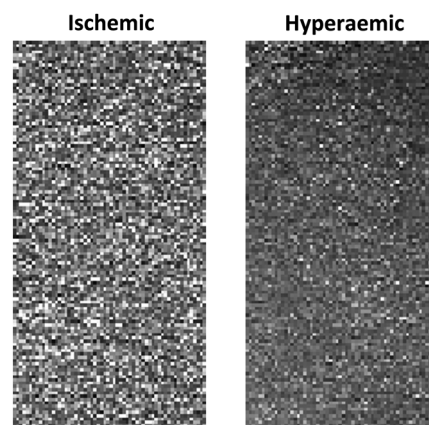


**Fig. 5** Raw speckle images from the surface of a finger tip. The left panel is taken when blood flow to the finger tip is temporally stopped. The speckle pattern shows high contrast between white and dark speckles. The right panel was taken immediately after blood flow was restored to the finger. The speckle pattern is blurred due to the motion of the red blood cells in the flowing blood.

intensity  $\langle I \rangle$  over an area of the image and provides a measure of the blurring of the speckle pattern,

$$K = \frac{\sigma_s}{\langle I \rangle} = \frac{\sqrt{\langle I^2 \rangle - \langle I \rangle^2}}{\langle I \rangle}. \quad (1)$$

Using perfectly monochromatic and polarized radiation, the speckle contrast of a static target  $K = 1$ . In practice, speckle contrast is less than one. Decreasing values of speckle contrast correspond to shorter speckle decorrelation times and therefore faster moving scattering centers. When interested in applying this technique to a spatially heterogeneous target,  $K$  is calculated over small subregions of the single frame, usually  $n \times n$  blocks of pixels, where block sizes typically range from  $5 \times 5$  to  $10 \times 10$ . Often a polarizer is used in front of the detector to help reject specular reflection and therefore increase the contrast of the measured speckle pattern. The integration time of the camera needs to be adjusted to match the speckle decorrelation time of interest. Integration times much longer than the speckle decorrelation times lead to a fully blurred image ( $K = 0$ ) while integration times much shorter than the decorrelation times lead to a speckle contrast approaching the value of a stationary speckle pattern. An integration time within these extremes and on the scale of the speckle decorrelation time is typically used. Longer integration times within this window can lead to camera noise adversely affecting the measured speckle contrast. A detector should be selected that has a low noise profile for the integration time(s) being used. For perfusion measurements, integration times are typically on the order of 2 to 10 ms. For best results, the speckle and pixel size should be on the same order. Speckle size is dependent on the wavelength of light ( $\lambda$ ), the  $f$ -number of the lens system, and the magnification ( $M$ ):

$$d = 1.2(1 + M)\lambda f. \quad (2)$$

Thus, the user can vary the integration time, magnification,  $f$ -stop, and illumination intensity to optimize the speckle contrast for the flow phenomenon of interest and the camera pixel and noise specifications. The method above is usually referred to as laser speckle contrast analysis (LASCA).<sup>74</sup> The temporal equivalent of LASCA is often referred to as laser speckle imaging (LSI).<sup>75</sup> LSI acquires a series of image frames in rapid succession and calculates the speckle contrast of a pixel over a sequence of images. When spatial statistics are used, as in LASCA, there is a subsequent loss in spatial resolution, while the use of temporal statistics in LSI leads to a loss in temporal resolution. LSI has the advantage that the temporal laser speckle contrast value is unaffected by the stationary part of the speckle pattern. Various combinations of spatial and temporal pixel statistics have been proposed to quantify speckle variance from a spatiotemporal series of speckle patterns.<sup>71-73</sup> These methods offer a compromise between LASCA and LSI.

Considerable effort has been made to extract a speed or a measure of flow based on the speckle variance. Goodman reported the relationship between the spatial variance of a time-averaged dynamic speckle pattern  $\sigma_s^2(T)$  and the temporal fluctuation statistics of speckle patterns over an integration time,  $T$ :<sup>76</sup>

$$\sigma_s^2(T) = \frac{2}{T} \int_0^T \left(1 - \frac{\tau}{T}\right) g_2(\tau) d\tau. \quad (3)$$

The measured spatial variance is generally given in terms of the intensity temporal autocorrelation function,  $g_2(\tau)$ , of a single speckle where  $\tau$  is the lag time. The Siegert relation is used to describe the relationship between the intensity and electric field temporal autocorrelation function,  $g_1(\tau)$ :

$$g_2(\tau) = 1 + \beta |g_1(\tau)|^2. \quad (4)$$

Based on different models relating the velocity of scattering centers to the electric field temporal autocorrelation function, the measured speckle contrast and the velocity of scattering centers can be derived.<sup>76-78</sup>

Red blood cells are efficient light scattering centers within tissue so the resulting speckle patterns from perfused tissue contain information about blood flow in the form of speckle variance or blur. However, as discussed above, to extract blood flow measurements from the speckle statistics requires knowledge of the underlying velocity distribution, the fraction of moving scattering centers, and the degree of multiple scattering. Due to the complexities of tissue vascular networks, the optical properties of surrounding tissues and the subsequent assumptions and simplifications necessary to extract absolute velocities from speckle statistics, it is generally accepted that speckle contrast is indicative of relative blood flow or a measure of blood perfusion in tissue. Figure 6 shows a sequence of laser speckle images of a finger captured before and after immersion in ice water. The images clearly show the response of the superficial circulation of the finger tip to the cold challenge and the subsequent hyperemia following the removal of the cold stimulus.

Despite the qualitative nature of these measurements, for the assessment of wound perfusion, speckle imaging methods are particularly useful in that they provide perfusion information over an area of tissue fast enough not to be overly confounded by patient movement or breathing. They have the added advantages of being relatively cheap and easy to implement, and recently commercial instrumentation has become available. The major practical challenge with this method is its sensitivity to movement or motion unrelated to blood flow. Further advances in signal processing leading to improved real-time image registration and motion filtering will reduce the confounding effects of patient motion on laser speckle perfusion measurements. Figure 7 shows a color digital picture and a corresponding perfusion speckle image of a foot with arterial insufficiency. Areas of hypo- and hyperperfusion are clearly visible in the speckle image of the compromised foot. Recently laser speckle flow measurements have been compared to ICG angiography<sup>79</sup> and spatial frequency domain imaging,<sup>80</sup> and a clinical study has been reported using laser speckle to assess perfusion in free flap transfers.<sup>81</sup>

### 5.3 Vascular Mapping and Perfusion Measurements with Optical Coherence Tomography

Optical coherence tomography (OCT), originally demonstrated in 1991, is a noninvasive depth-resolved biomedical imaging modality. It has better resolution than ultrasound and achieves deeper penetration than confocal microscopy, and it can provide distinctive morphological information over larger tissue regions

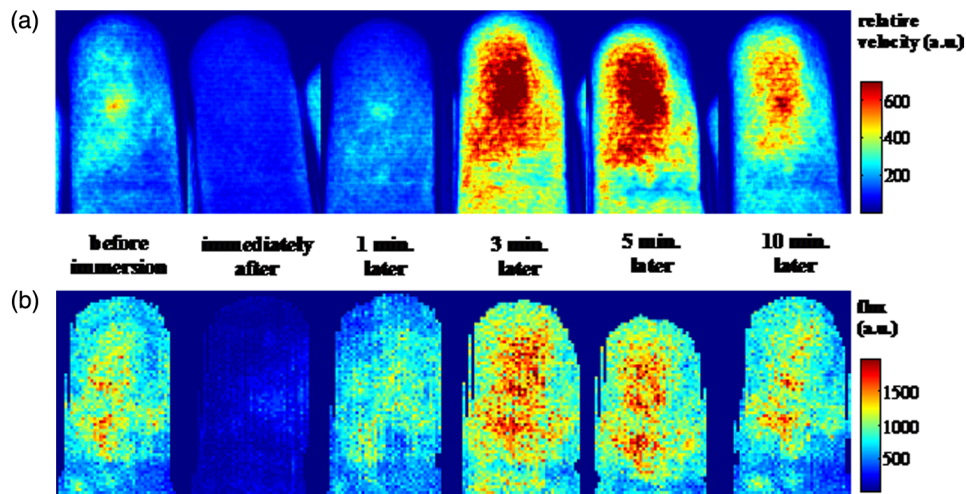


**Fig. 6** A sequence of false color laser speckle images of a finger tip before and after immersion in ice water. During the cold challenge superficial perfusion is reduced. Once the challenge is resolved perfusion increases dramatically to restore hemostasis. Perfusion remains elevated up to 10 min following this challenge.

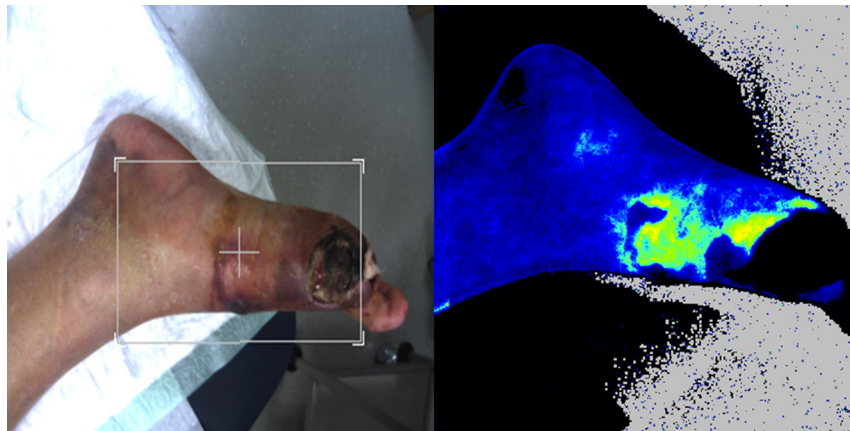


**Fig. 7** Left panel is a digital color picture of the foot of a patient with arterial insufficiency. Right panel is a full-field laser speckle contrast image (PeriCam PSI system, Perimed AB) of the same foot pictured in the left panel. The eschar on the wound may be giving false low perfusion readings. Wound debridement is generally recommended before perfusion imaging.

than nonlinear optical microscopy.<sup>82-84</sup> Thus, OCT has been evaluated for the identification of characteristic architectural changes that correlate with the histological phases of cutaneous wound healing.<sup>85,86</sup> OCT is a low coherence light interference-based technique. The OCT signal is produced by the superposition of multiple backscattered optical fields which gives rise to accompanying speckle noise. In anatomical OCT imaging, coherent speckle noise is undesirable as it can obscure structural features. Various strategies have been proposed to reduce speckle noise in anatomical OCT imaging.<sup>87-90</sup> However, OCT speckle conveys information on the structure and motion of scattering centers within the sample.<sup>91</sup> Analogous to LASCA and LSI, measures of speckle variance or decorrelation can be obtained from OCT images.<sup>92</sup> While LASCA or LSI provide two-dimensional (2-D) perfusion imaging, they cannot provide the depth-resolved perfusion map that OCT-based methods are capable of generating. Figure 8 shows a simple OCT decorrelation method to distinguish moving from static features in an image. In this demonstration, the cross-correlation between two

consecutive OCT B-scan images is calculated. Within the OCT images are cross sections of two capillary tubes. One tube is filled with 4% intralipid, and the second tube is empty. Using an intensity threshold mask to segment the regions of signal from the noise portions of the original OCT image and multiplying the cross-correlation image with the binary intensity threshold image mask isolates the features which have moved between the two frames from the static features in both frames.

Although speckle decorrelation methods cannot provide information on the flow velocity or direction, they are sensitive to the motion of red blood cells and hence highlight the local vascular density. In wound healing, rapid angiogenesis during the inflammatory and proliferative phases and the eventual revision of neovascular networks during remodeling have a profound influence on healing progression and scarring.<sup>93</sup> Vascular mapping with OCT provides a means to quantify angiogenesis and follow its progression over the healing phases.

A clinical assessment of vascularity in burn scars of human patients *in vivo* has been demonstrated by using speckle

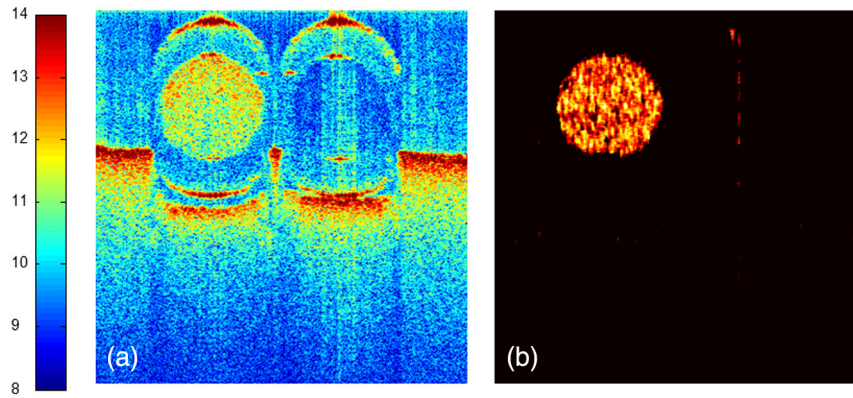


**Fig. 8** (a) OCT B-scan (log of intensity) of two 1 mm outer diameter capillary tubes laying on a cork surface. The left tube contains 4% intralipid and the right tube is empty. (b) The cross-correlation image between two consecutive B-scans using a  $7 \times 7$  spatial window. To eliminate noise artifacts, the cross-correlation image is multiplied by a binary intensity mask using threshold intensity of  $>1e4$  of the original OCT B-scan. Only the moving intralipid particles within the filled capillary tube appear in the decorrelation map (7B).

decorrelation OCT.<sup>94</sup> Their quantitative vascular parameters showed increased vascular density and enlarged vessel diameter in scar tissue compared with normal skin. Several vascular contrast OCT methods have been developed.<sup>92,95–101</sup> These include speckle variance OCT and phase- or intensity-based Doppler variance OCT for mapping vascular networks in human skin and the vascular structure in tumors. Figure 9 shows an experiment following a wound from day zero (the day of wound formation) to day 14 of healing. Vascular contrast is obtained by calculating the variance of the Doppler frequency spectrum. Figure 9(a) shows the maximum intensity projection from the

surface to  $\sim 1.2$ -mm depth in normal skin. Figure 9(b) shows a similar vascular map taken immediately after wound formation while Figs. 9(c), 9(d), and 9(e) show vascular maps taken 3, 6, and 14 days after wound formation. Vessel widths as small as  $15 \mu\text{m}$  can be resolved by calculating the variance of the Doppler frequency spectrum. The wound healed from the edge, finally reaching the center. Extensive angiogenesis at the edge of the wound is evident from the increased vasculature density and vessel diameter at the edge of the wound compared to the center in the days following wound formation, Figs. 9(c) and 9(d). Starting from the sixth day, the area of scar increased

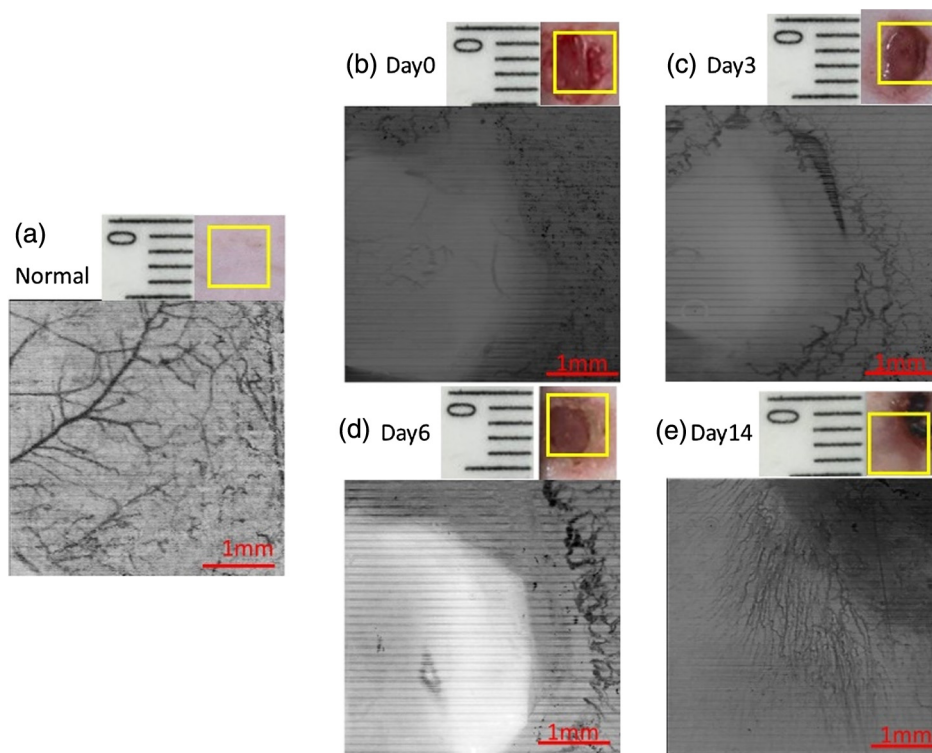


**Fig. 9** Representative *en face* maximum intensity projection reconstructions from the surface to 1.2 mm depth of the 3-D vascular maps. Vascular maps, 7(a) normal skin, (b) day 0—wound formation, (c) day 3, (d) day 6, and (e) day 14.

toward the center of the wound. After 14 days, the wound appears to have reached the remodeling phase. The vascular map in Fig. 9(e) is consistent with this observation.

## 6 Near-Infrared Methods to Assess Arterial Sufficiency

In peripheral vasculature, the systole–diastole phases of the cardiac cycle result in a modulated dilation and contraction of arteries.<sup>102–104</sup> This small difference in blood volume between the systolic and diastolic phases of the cardiac cycle produces a modulation in the measured attenuation of light by well perfused tissue (see Fig. 10). The pulse, due to blood volume change, is heavily dampened in the highly compliant venous system. Therefore, the modulation in the optical attenuation due to the pulsatile blood volume change is largely localized in the arterial compartment of the circulatory system. This well-known phenomenon is exploited in pulse oximetry and photoplethysmography (PPG) to provide information about the arterial blood supply to the underlying tissue. The measurement of PPG “pulses” at the toes and fingers is routinely performed in patients with peripheral vascular disease (PVD) to confirm the extent of compromised circulation in the extremities<sup>102–106</sup> as well as being helpful in assessing the success of revascularization procedures,<sup>107</sup> and predicting wound healing following amputation.<sup>108</sup> PPG offers a simple, reliable,<sup>109</sup> and effective noninvasive means to detect a robust arterial supply to the extremities by measuring the depth of the pulsatile modulation of the optical attenuation. Strong PPG pulses at the toes and feet suggest a good arterial supply of blood to the extremity. This turns out to be an important parameter in the management of PVD patients.

The modulation depth of the PPG signal is an indicator of the robustness of the arterial supply of blood to the underlying tissue. However, the shape of the PPG waveform conveys additional information.<sup>110</sup> The temporal contour of the PPG signal is similar to the pulse waveform as measured by an arterial blood pressure catheter inserted percutaneously into a peripheral artery. The peak systolic and diastolic pressure points as well as the sharp incisura that coincides with the closure of the aortic valve and the cessation of ventricular ejection are clearly visible in the noninvasive optical reflectance PPG signal. Figure 10 shows a typical reflectance PPG configuration and a

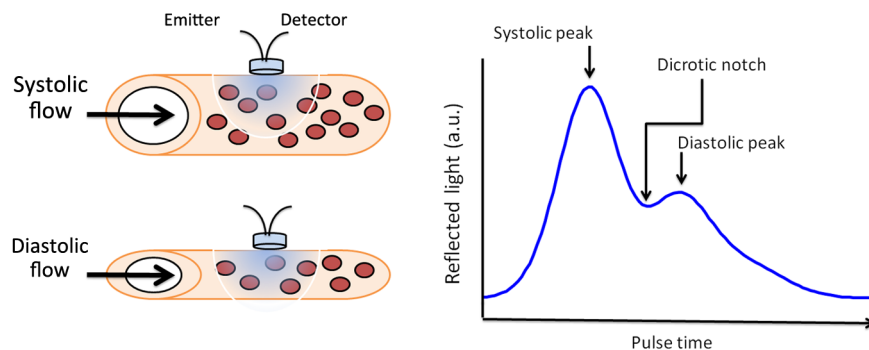


**Fig. 10** The PPG signal consists of the portion of the detected back reflected light being modulated by the pulsatile flow of blood through the arteries. Elastic arteries absorb energy over the systolic component of the cardiac cycle and expand, releasing that energy over the diastolic phase. A prototypical PPG signal can differentiate these two phases. The anacrotic phase appears as a rapid increase in the PPG signal and is associated with systole. The catacrotic phase, which is the falling portion of the PPG signal, is associated with diastole and wave reflections from the peripheral vascular system. The intensity and shape of the PPG signal conveys diagnostic information.

prototypical PPG signal. The shape of the PPG pulse waveform depends on cardiac output and the compliance of the vascular bed being interrogated. The natural stiffening of arteries that accompanies age, as well as microvascular effects associated with hypertension and diabetes, can have a profound effect on the PPG pulse waveform. The amplitude of the systolic peak, pulse width, pulse area, time between the systolic and diastolic peaks, peak to peak interval, and pulse interval have been used as diagnostic parameters for local and systemic vascular health. Analysis of these waveforms and their transit times can help detect cardiovascular pathologies such as hypertension and diabetes as well as potentially indicate a patient’s risk for cardiovascular disease. Clinically, the magnitude of the pulsatile modulation of the optical signal correlates with the sufficiency of the arterial supply of blood to peripheral tissue, while the PPG pressure waveform can be used to assess peripheral resistance, arterial compliance, and wave propagation, providing clues to the vascular health of the patient. Recent technical advancements in PPG measurement have been to use fast imaging methods to capture the pulsatile modulation over an area of tissue<sup>111</sup> and to develop consumer oriented PPG wearables.<sup>112</sup> The simplicity of this technology and the move toward consumer wearable devices suggests a further role of PPG technologies in home care assessments of vascular disease and wounds to the extremities.

## 7 Near-Infrared Methods to Assess Microvascular Oxygenation

NIR tissue oximetry is closely related to pulse oximetry in that it relies on the measuring the reflected or transmitted light from tissue at wavelengths where the oxygenated and deoxygenated forms of hemoglobin absorb light to different degrees. By measuring, at these wavelength regions, the degree of light attenuation by tissue and understanding the light absorption properties of the different forms of hemoglobin at those wavelengths, a model can be derived to determine the relative proportion of oxygen-carrying to deoxygenated hemoglobin. This proportion is known as hemoglobin oxygen saturation. Given that hemoglobin is the dominant oxygen carrier in blood, hemoglobin oxygen saturation is a good measure of the oxygen available to tissue.

The complexities of tissue lead to challenges in developing a quantitative model to accurately predict the concentrations of the oxygenated and deoxygenated forms of hemoglobin. A simple yet reliable approach relies on a differential measurement of the hemoglobin oxygen saturation. The measure light remittance between a “baseline” and “activated” state can be analyzed in terms of a modified Beer–Lambert (MBL) approach to provide an estimate of the difference in hemoglobin oxygenation between the two states.<sup>1</sup> Pulse oximetry uses this approach by measuring the difference of remitted light at the systolic and diastolic phases of the cardiac cycle at a “red” and “NIR” wavelength. The modulation of the remitted light due to the pulsatile blood volume change is largely localized in the arterial compartment of the circulatory system, and the measured oxygenation,  $S_pO_2$ , can be related to the systemic arterial hemoglobin oxygenation,  $S_aO_2$ . The pulse modulated change in blood volume decreases as blood descends down the vascular tree through the arteries into the arterioles, the capillary network, and the venous system. PPG and pulse oximetry provide little insight about the oxygen supply to small arterioles, capillaries, and veins because of their reliance on the pulse modulated component of the optical attenuation signal. In addition, wounds often have an incompetent arterial supply with muted pulses, making PPG and  $S_pO_2$  measurements unreliable at the location of the wound. However, oximetry methods that are based on the static component or sample both the static and pulse modulated components of the optical attenuation signal will sample the entire vascular bed of the underlying tissue. These measures provide a general estimate of mixed arterial and venous blood oxygenation in the volume of tissue interrogated by the device and are more indicative of the oxygen supply at the microvascular level. These measures are often referred to as tissue oxygenation measurements or  $S_tO_2$ .

An obvious differential measurement scheme for measuring wound tissue oxygenation is to compare the oxygenation at the wound site to a nearby uninvolved site. However, the optical properties of the wound are likely to be vastly different from the uninvolved native tissue, often confounding a direct comparison between the different tissues. Tissue in general is heterogeneous, complex, and dynamic. All of these factors impact the light absorption and scattering properties and hence the transport of light. Scattering is largely dictated by the structural properties of tissue such as boundaries and interfaces, cell count, particle size, and shape. The light absorption characteristics of tissue are determined by the types and concentrations of constituent biomolecules that intrinsically absorb light in the NIR wavelength range. Whether using a direct or differential measurement scheme, a quantitative measurement of wound hemoglobin oxygen saturation requires a detailed understanding of the optical properties of the underlying tissue and the appropriate inverse model to transform measurements of light attenuation into measures of hemoglobin concentration.

Two general strategies used to model the propagation of light in tissue are statistical Monte Carlo (MC) simulation of photon trajectories and deterministic calculations based on the Boltzmann transport equation. The Boltzmann transport equation, also known as the radiative transport equation (RTE), is formulated in terms of a conservation law that accounts for the gains and losses of photons due to scattering and absorption.<sup>113–116</sup> It describes the balance between the number of photons entering and leaving an infinitesimal volume element in a given direction as well as the losses through

absorption. The RTE admits no closed form solutions that are relevant to *in vivo* measurement conditions; therefore, considerable effort is being devoted to developing efficient numerical methods to solve the multidimensional RTE and the formulation of accurate and tractable approximations to the RTE. The diffusion equation (DE) is a low-order approximation to the RTE that essentially assumes nearly isotropic radiance. It is applicable when scattering dominates absorption and where the scattering mean free path ( $1/\mu_s$ ) is small compared with the distance and time of propagation. The DE has analytical solutions for a number of simple geometries, while numerical methods such as finite difference and finite element methods can be used to solve the DE for more complex geometries. The DE and extensions of the equation are used extensively to provide fast and convenient descriptions of light propagation in diffusive media such as tissue.<sup>117,118</sup>

MC methods simulate the path of individual photons through the tissue using probability models describing the probability of a scattering event and the resulting scattering angle based on the scattering coefficient, the scattering phase function, and the anisotropy of scattering of light in the area of the tissue where the photon is located.<sup>119</sup> A series of interaction steps is calculated by resampling the distribution of scattering lengths and scattering angles independently of the previous step, resulting in a trajectory of the photon in the medium. The series of steps results in a random walk of the photon that terminates once it exits the medium or is annihilated through absorption. The net distribution of all the photon paths can be used to derive approximations to remittance, transmittance, and absorption of light given a particular measurement geometry and sample morphology. The statistical nature of MC simulation requires that many photon trajectories need to be generated and averaged before the results can begin to model experimental observations, making MC methods computationally expensive. Recent trends look to accelerate the computations using massive parallel computing approaches as well as incorporating more realistic models of tissue morphology into the MC method.<sup>120</sup>

In addition to the challenges in developing rigorously accurate inverse models, the optical properties of tissue and in particular the properties of injured or healing tissue are not well established. The diverse etiology and types of wounds and the dynamic healing process compounds the problem of deriving omnibus optical properties broadly applicable to wounds and healing tissue. Despite these complications, approximate and sometimes even crude models with generic optical property parameters can provide useful semiquantitative or qualitative measurements of microvascular oxygenation at the wound site. The utility of NIR spectroscopy and in particular imaging is being explored to determine peripheral vascular perfusion,<sup>121–125</sup> burn injury assessment,<sup>126–129</sup> as well as the assessment of oxygenation of superficial tissues during surgery, postsurgery, and during healing.<sup>130–136</sup> Figure 11 shows a tissue oxygenation image derived from a four-wavelength multispectral reflectance image of the planter portion of the foot that has a diabetic ulceration. The ulceration has a very low value of oxygenation compared to the surrounding tissue.

## 8 Optical Methods to Assess Extracellular Matrix Formation

Functional and esthetic outcomes of the healing wound are critically dependent on the formation and organization of the extracellular matrix. Two optical methods, polarization-sensitive

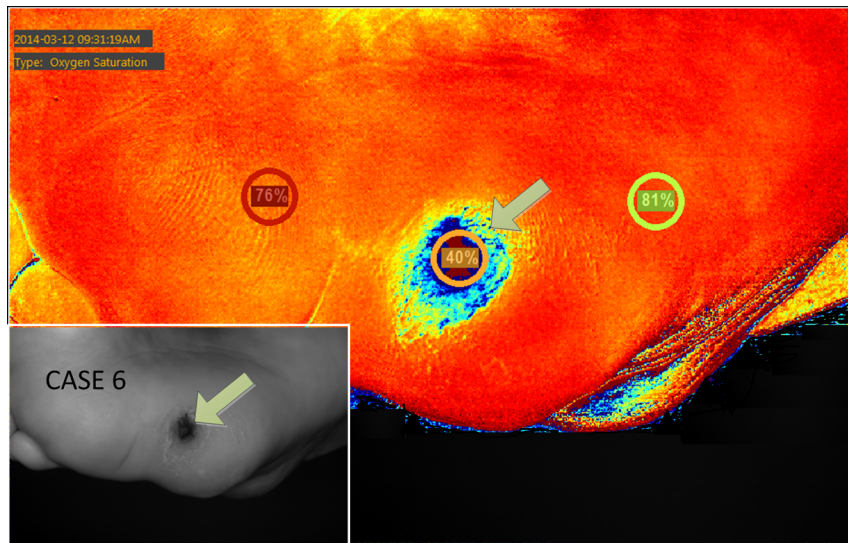


**Fig. 11** Tissue oxygenation image (using the KC-103, Kent Imaging) of the right planter foot with a diabetic foot ulcer showing limited healing. The wound bed (pointed out by the arrow) shows a significantly lower tissue oxygenation than the surrounding uninvolved tissue. The insert is a black and white picture of the same area of the foot.

optical coherence tomography and second harmonic generation, are well suited to studying the organization of collagen.

### 8.1 Polarization-Sensitive Optical Coherence Tomography

Polarization-sensitive optical coherence tomography (PS-OCT), first demonstrated by Hee et al.,<sup>137</sup> provides noncontact and high-resolution tomographic image as well as determining the retardation and birefringence from tissues. Birefringence characterizes the differential speed of propagation between two orthogonal polarized states of light in a medium. Birefringence is exhibited in media containing ordered arrays of anisotropic structures that are smaller than the wavelength of the incident light. Collagen fibers and bundles are strongly birefringent. Thus, PS-OCT is a three-dimensional (3-D) imaging method that is sensitive to the degree of collagen organization on a 10- to 100- $\mu\text{m}$  length scale, and both collagen content and the orientation of collagen fibers are correlated to the change of phase retardation in PS-OCT. Structural changes of collagen and collagen organization play a significant role during wound healing.<sup>138</sup> PS-OCT can be used to noninvasively monitor and evaluate the wound healing process involving the local variations of the structural integrity and organization of collagen fibers.<sup>139</sup> For example, quantification of the normalized birefringence and mean phase retardation during wound healing using PS-OCT has been demonstrated in an *in vivo* rabbit auricle model in 2006.<sup>140</sup> From monitoring the changes in birefringence over the healing process, they found an increase in birefringence with time. Gong et al.<sup>141</sup> assessed the collagen structure of different human scars using an enface birefringence map calculated from the rate of change of the phase retardation. They also confirmed the correlation of birefringence with scar type. Since scars consist mainly of poorly reconstructed thick parallel bundles collagens they show distinct PS-OCT characteristics compared to normal skin. Figure 12 shows our *in vivo* experiment after 14 days of wound healing. The figure includes an enface map of the measured birefringence [Fig. 12(b)], a representative

B-mode intensity image [Fig. 12(c)], and a retardation B-mode image [Fig. 12(d)] across a scab (right part) and region with slough (left part). The scab consist mainly of necrotic tissue and shows poor or no birefringence while the healed region has extensive collagen regeneration contributing to the large phase retardation as indicated by the arrows in Fig. 12(d).

### 8.2 Nonlinear Optical Imaging

The optical detection of backscattered second harmonic generation (SHG) and two-photon excited fluorescence (TPEF) from NIR laser illumination of a wound site offers a powerful 3-D imaging method for extracellular collagen and elastin.<sup>142–145</sup> Fibrillar collagen, especially type I, produces strong SHG signals due to its noncentrosymmetric molecular structure and is one of the most well-documented SHG generators in tissue.<sup>146–148</sup> As a label-free imaging technique, SHG imaging can detect and allow for the visualization of collagen deposits as well as provide information on the textural characteristics of these deposits at higher resolution (i.e., submicron) than PS-OCT.<sup>149</sup> In a typical microscope setup, collagen SHG images are generated by raster scanning a focused beam of NIR femto-second laser light (e.g., 780 to 800 nm) into the tissue via an objective lens. The nonlinear optical signal is generated in the region of the focal spot of the laser where the electromagnetic field strength is sufficient to efficiently generate nonlinear optical processes such as harmonic generation and multiphoton fluorescence. The SHG signal is collected at exactly half the incident wavelength using narrow band optical filtering. A single SHG collagen image may cover an area from 100 to 800  $\mu\text{m}$  depending on the lens system used while the axial resolution is typically on the single-micron scale. The optical sectioning nature of this method enables 3-D collagen imaging by stacking 2-D SHG images taken along the depth axis of the tissue sample. Using the same excitation source but monitoring the TPEF (excitation = 800 nm and emission =  $530 \pm 20$  nm), elastin can be detected simultaneously. Near-infrared excitation enables deeper optical sampling with less thermal damage within the

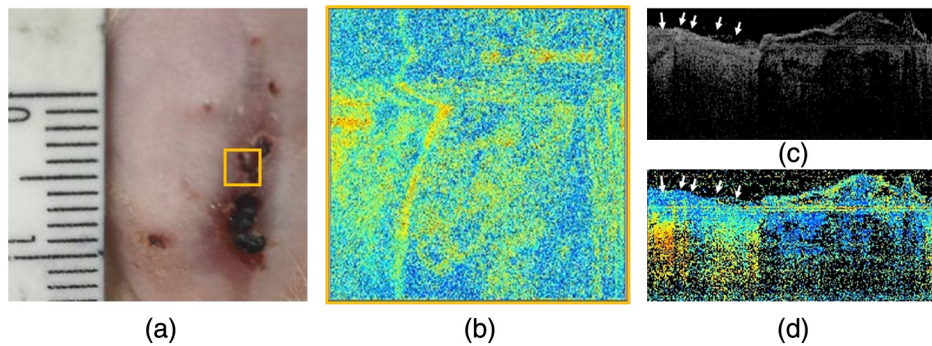


**Fig. 12** PS-OCT imaging across a wound including a scab region (right part) and region with slough (left part). (a) Photograph of the wound with the portion of the scab and region with slough included in the PS-OCT scan as indicated by the square in the photograph. (b) *En face* birefringence map calculated from the PS-OCT image. (c) and (d) Cross-sectional backscattered intensity and phase retardation images across the scab boundary, respectively. Arrows in the diagram point to regions of tissue exhibiting large phase retardation which correspond to areas with increased collagen deposits.

bulk skin tissue for SHG and TPEF imaging. Figure 13 shows a schematic illustration of the optical sectioning process in non-linear optical (NLO) imaging as well as energy level diagrams for SHG and TPEF.

While skin biochemistry can be investigated with the assistance of extrinsic fluorescent contrast agents, it is NLO imaging that can take the full advantage of the intrinsic optical signature of the molecular components such as collagen, elastin, and keratin—the major components in skin. Collagen remodeling plays a critical role in determining the strength and appearance of a healed wound. Therefore, SHG imaging of collagen can study wound closure and scar formation. Navarro et al.<sup>150</sup> and Luo et al.<sup>151</sup> incorporated SHG imaging to monitor wound closure in swine and mice models, respectively, to gain deeper understanding of the healing process. Brewer et al.<sup>152</sup> was the first to investigate human scarring using excised normal and

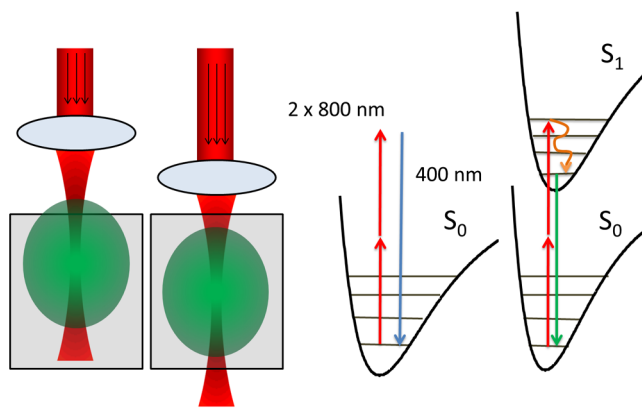


**Fig. 13** (Left half of image) NLO processes require high electric field strengths and are only efficiently generated in the focal waist of the exciting laser. By moving the position of the focal spot within the medium, 3D volumetric NLO of the medium can be obtained. (Right half of image) Energy level diagrams of SHG in collagen and two-photon excited fluorescence (TPEF) of elastin. SHG at 400 nm can be generated by type I and II collagen. Imperfect phase matching gives rise to a distribution of forward and backward scattered second harmonic light, which is further diffused as it traverses through light scattering tissue. For TPEF to occur, the two 800 nm photons are in resonance with the ground ( $S_0$ ) and excited singlet ( $S_1$ ) electronic states of elastin. Stokes shifted isotropic fluorescence emission occurs as the electron relaxes from  $S_1$  to  $S_0$  state of elastin.

keloid scar tissues and found significant collagen density differences between the tissues. Comparing biopsies taken from hypertrophic and keloid scars, Meshkinpour et al.<sup>153</sup> also reported morphological differences in the local collagen microstructures revealed by SHG images. Chen et al.<sup>154</sup> also reported imaging of human hypertrophic scars using TPEF and SHG. Later Da Costa et al.<sup>155</sup> used SHG imaging to compare live human keloids and normal facial tissue and observed a swirling collagen morphology in keloids, compared with the typical wavy collagen structure in normal skin. Chen et al.<sup>156</sup> reported that based on SHG and TPEF data of keloid scar tissue samples, the collagen content increased in both upper and deeper dermis while a higher density of elastin only appeared in the deep dermis as opposed to normal skin. Such observation spurred studies that used the intensity ratio of TPEF (elastin) to SHG (collagen) signals to classify scar types.<sup>157,158</sup> These studies provided new insight into the molecular processes underlying different types of scar formation and thus provide a tool to help guide the development of new treatment strategies to reduce scarring and improve the mechanical properties of healed wounds. Figure 14 shows an example of SHG signals from healed infarcted cardiac tissue that was untreated compared with stem cell treated tissue.

An area of growing interest is the development of collagen classification metrics.<sup>159,160</sup> These metrics provide for an objective and thus more reliable identification of various extracellular collagen morphological motifs based on SHG image statistics.<sup>161,162</sup> Figure 15 shows several collagen structure motifs that have distinct texture scores. By combining image processing methods with NLO imaging, scar borders can be objectively delineated and different scarring processes can be differentiated with a higher level of accuracy and confidence.<sup>163</sup>

While the majority of the NLO imaging applied to dermatology/wound healing is still exploratory in nature, recently Koenig et al.<sup>164,165</sup> have made important advances in the development of a clinical multiphoton imaging device. A series of clinical devices based on various NLO imaging methods have obtained FDA approval for *in vivo* study of skin biochemical morphology.<sup>166</sup> Their technology uses a GRIN lens to allow imaging from within tissue to study the biochemical morphology of the extracellular matrix, thus providing a unique perspective on scar imaging.<sup>167</sup> This technology could be an ideal candidate to monitor the wound healing process at the molecular level during remodeling.

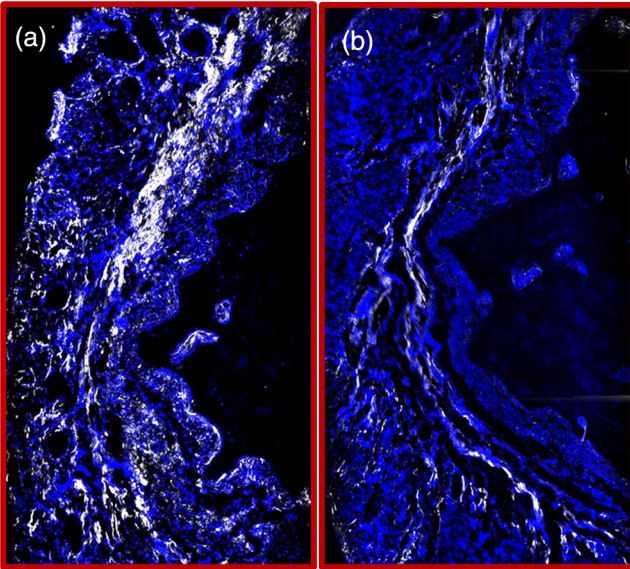


**Fig. 14** Second harmonic (white) and two-photon excited fluorescence (blue) signals from biopsied infarcted myocardium with (a) no treatment and (b) a stem cell treatment. Excitation wavelength is at 800 nm. Collagen SHG signal was collected using a  $400 \pm 5$  nm band-pass filter in the forward direction while the DAPI-TPEF signal was collected in the backscattered (epi) direction through a  $505 \pm 50$  nm filter. The stem cell treated infarcted tissue shows less collagen but with a more ordered structure compared to the more random collagen structure of the untreated infarcted tissue.

## 9 Conclusion

Instrumental methods are increasingly being relied upon to provide objective metrics of healing. Tissues have a number of useful optical properties in the NIR region of the electromagnetic spectrum; therefore, technologies that employ NIR light form a prominent contingent among the existing and emerging devices. NIR light is nonionizing, and therefore the threshold for tissue damage is relatively high, making them generally safe to use on people. Relative to the neighboring visible and infrared regions of the electromagnetic spectrum, NIR light is weakly absorbed by tissue but highly scattered. Therefore, it can be used to interrogate tissue well into the dermis. Tissue melanin absorbs light more weakly across the NIR region compared with visible light, making NIR technologies applicable to a wider ethnic diversity of patients when wanting to sample beyond the epidermis. Red blood cells strongly scatter NIR light, and their motion or change in concentration imparts detectable alterations in the measured attenuation of light by perfused tissue. Hemoglobin, the dominant carrier of oxygen in blood, has distinct NIR light absorption spectra depending on whether oxygen is bound to the heme or not. Cutaneous collagen scatters light differently depending on its type and its organizational structure within the tissue. These intrinsic NIR optical properties of tissue can be exploited to provide information on perfusion, tissue oxygenation, vascular compliance, angiogenesis, and the structural characteristics of the extracellular matrix. All of these are relevant to the healing wound. In addition to these intrinsic NIR properties of tissues, significant research effort has led to a wide

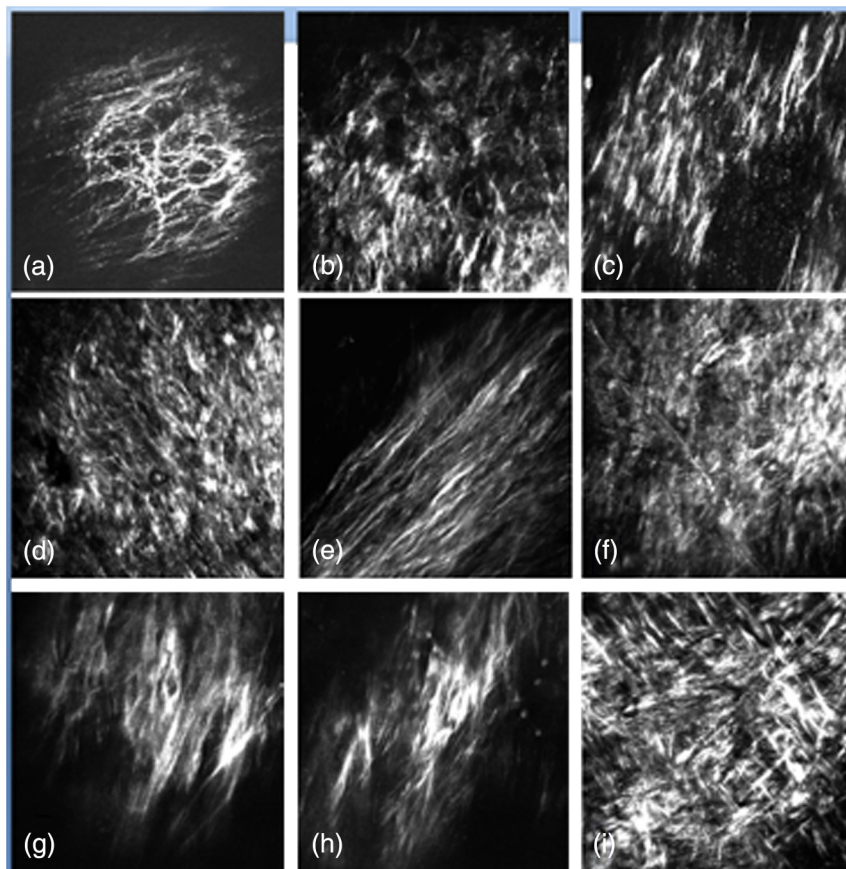


**Fig. 15** Structural motifs in second-harmonic collagen images of arterial tissue biopsies that have distinct texture properties based on gray level cooccurrence scores calculated for the images, labelled (a) to (i).

range of NIR fluorophores such as fluorescent quantum dots and nanoparticle constructs that can be used with targeting moieties such as antibodies to elucidate a wide range of biochemical processes within wounds. This opens the door to near-infrared based methods probing specific molecular facets of wound healing. On their own, near-infrared fluorophores, as exemplified by indocyanine green, can be used as flow tracers to assess wound perfusion.

The rapid progress in computing, connectivity, and photonics along with the economic scaling of those technological centerpieces, in confluence with the urgent drive toward cost containment within our health care systems, suggests we are poised for a technological revolution that will enable patient empowered wound monitoring outside of the traditional hospital setting. Taken together, NIR-based technologies can play a central role in this revolution, providing tools to assess wounds along the entire healing trajectory from hemostasis and inflammation to wound remodeling and scar formation.

## References

- M. G. Sowa and J. Friesen, "Near-infrared spectroscopy, in vivo tissue analysis by," in *Encyclopedia of Analytical Chemistry*, R. A. Meyers, Ed., John Wiley, Chichester (2013).
- J. Zarocostas, "Non-communicable diseases must have greater priority, says WHO," *BMJ* **339**, b2857 (2009).
- Home—UK Stem Cell Foundation, <http://www.ukscf.org/>.
- N. R. Barshes et al., "The system of care for the diabetic foot: objectives, outcomes, and opportunities," *Diabet. Foot Ankle*. **4**, 21847 (2013).
- S. Morbach et al., "Long-term prognosis of diabetic foot patients and their limbs: amputation and death over the course of a decade," *Diabetes Care* **35**, 2021–2027 (2012).
- D. G. Armstrong, J. Wrobel, and J. M. Robbins, "Guest editorial: are diabetes-related wounds and amputations worse than cancer?," *Int. Wound J.* **4**, 286–287 (2007).
- D. G. Armstrong et al., "Mind the gap: disparity between research funding and costs of care for diabetic foot ulcers," *Diabetes Care* **36**, 1815–1817 (2013).
- K. S. Chandan et al., "Human skin wounds: a major and snowballing threat to public health and the economy," *Wound Repair Regen.* **17**(6), 763–771 (2009).
- G. Broughton, II, J. E. Janis, and C. E. Attinger, "Wound healing: an overview," *Plast. Reconstr. Surg.* **117**, 1E-S (2006).
- T. Velnar, T. Bailey, and V. Smirolj, "The wound healing process: an overview of the cellular and molecular mechanisms," *J. Int. Med. Res.* **37**(5), 1528–1542 (2009).
- J. M. Reinke and H. Sorg, "Wound repair and regeneration," *Eur. Surg. Res.* **49**, 35–43 (2012).
- T. J. Koh and L. A. DiPietro, "Inflammation and wound healing: the role of the macrophage," *Expert Rev. Mol. Med.* **13**, e23 (2011).
- B. M. Delavary et al., "Macrophages in skin injury and repair," *Immunobiology* **216**, 753–762 (2011).
- P. Italiani and D. Boraschi, "From monocytes to M1/M2 macrophages: phenotypical vs. functional differentiation," *Front. Immunol.* **5**, 514 (2014).
- C. D. Mills and K. Ley, "M1 and M2 macrophages: the chicken and the egg of immunity," *J. Innate Immun.* **6**(6), 716–726 (2014).
- L. A. DiPietro, "Angiogenesis and scar formation in healing wounds," *Curr. Opin. Rheumatol.* **25**(1), 87–91 (2013).
- P. Olczyk, L. Mencner, and K. Komosińska-Vashev, "The role of the extracellular matrix components in cutaneous wound healing," *BioMed. Res. Int.* **2014**, 747584 (2014).
- B. Hinz et al., "Recent developments in Myofibroblast biology: paradigms for connective tissue remodeling," *Am. J. Pathol.* **180**(4), 1340–1355 (2012).
- A. Desmouliere, C. Chaponnier, and G. Gabbiani, "Tissue repair, contraction and the myofibroblast," *Wound Rep. Regen.* **13**, 7–12 (2005).
- T. A. Mustoe, K. O'shaughnessy, and O. Kloeters, "Chronic wound pathogenesis and current treatment strategies: a unifying hypothesis," *Plast. Reconstr. Surg.* **117**(7 Suppl.), 35S–41S (2006).
- R. G. Frykberg and J. Banks, "Challenges in the treatment of chronic wounds," *Adv. Wound Care.* **4**(9), 560–582 (2015).
- G. DiPietro and L. A. DiPietro, "Factors affecting wound healing," *J. Dent. Res.* **89**(3), 219–229 (2010).
- J. Li, J. Chen, and R. Kirsner, "Pathophysiology of acute wound healing," *Clin. Dermatol.* **25**, 9–18 (2007).
- V. Falanga, "Wound healing and its impairment in the diabetic foot," *Lancet* **366**(9498), 1736–1743 (2005).
- D. G. Armstrong et al., "It's not what you put on, but what you take off: techniques for debriding and off-loading the diabetic foot wound," *Clin. Infect. Dis.* **39**(Suppl 2), S92–S99 (2004).
- L. X. Zhan et al., "The society for vascular surgery lower extremity threatened limb classification system based on Wound, Ischemia, and foot Infection (WIFI) correlates with risk of major amputation and time to wound healing," *J. Vasc. Surg.* **61**(4), 939–944 (2015).
- D. G. Armstrong and J. L. Mills, "Juggling risk to reduce amputations: The three-ring circus of infection, ischemia and tissue loss-dominant conditions," *Wound Med.* **1**, 13–14 (2013).
- C. K. Sen, "Wound healing essentials: let there be oxygen," *Wound Repair Regen.* **17**(1), 1–18 (2009).
- S. Schremi et al., "Oxygen in acute and chronic wound healing," *Br. J. Dermatol.* **163**, 257–268 (2010).
- E. Landis, "Micro-injection studies of capillary blood pressure in human skin," *Heart* **15**, 209–228 (1930).
- S. Tricklebank, "Modern trends in fluid therapy for burns," *Burns* **35**, 757–767 (2009).
- C. W. J. Oomens et al., "Pressure induced deep tissue injury explained," *Ann. Biomed. Eng.* **43**(2), 297–305 (2014).
- R. Agha et al., "A review of the role of mechanical forces in cutaneous wound healing," *J. Surg. Res.* **171**, 700–708 (2011).
- R. Ogawa, "Mechanobiology of scarring," *Wound Repair Regen.* **19**(S1), S2–S9 (2011).
- G. Zhao et al., "Biofilms and inflammation in chronic wounds," *Adv. Wound Care.* **2**(7), 389–399 (2013).
- S. Kose and A. Waseem, "Keloids and hypertrophic scars: are they two different sides of the same coin?," *Am. Soc. Dermatol. Surg.* **34**, 336–346 (2008).
- C. Huang et al., "Keloids and hypertrophic scars: update and future directions," *J. Plast. Reconstr. Surg. Global Open* **1**(4), e25 (2013).
- L. A. DiPietro, "Angiogenesis and scar formation in healing wounds," *Curr. Opin. Rheumatol.* **25**, 87–91 (2013).
- C. Tziotziou, C. Profyris, and J. Sterling, "Cutaneous scarring: pathophysiology, molecular mechanisms and scar reduction therapeutics," *J. Am. Acad. Dermatol.* **66**, 13–24 (2012).
- T. R. Dargaville et al., "Sensors and imaging for wound healing: a review," *Biosens. Bioelectron.* **41**, 30–42 (2013).
- P. Salvo et al., "The role of biomedical sensors in wound healing," *Wound Med.* **8**, 15–18 (2015).
- S. M. Daly and M. J. Leahy, "Go with the flow: a review of methods and advancements in blood flow imaging," *J. Biophotonics* **6**(3), 217–255 (2013).
- J. Caesar et al., "The use of indocyanine green in the measurement of hepatic blood flow and as a test for hepatic function," *Clin. Sci.* **21**, 43–57 (1961).
- B. F. Hochheimer, "Angiography of the retina with indocyanine green," *Arch. Ophthalmol.* **86**, 564–565 (1971).
- J. T. Alander et al., "A review of indocyanine green fluorescent imaging in surgery," *Int. J. Biomed. Imaging* **2012**, 1–26 (2012).
- D. Grosenick, H. Wabnitz, and B. Ebert, "Recent advances in contrast-enhanced near infrared diffuse optical imaging of diseases using indocyanine green," *J. Near Infrared Spectrosc.* **20**, 203–221 (2012).
- E. M. Sevcik-Muraca, "Translation of near-infrared fluorescence imaging technologies: emerging clinical applications," *Ann. Rev. Med.* **63**, 217–231 (2012).
- J. M. Green et al., "Intraoperative fluorescence angiography: a review of applications and outcomes in war-related trauma," *Mil. Med.* **180**(3 Suppl), 37–43 (2015).
- S. Wipper et al., "Intraoperative quality control in vascular surgery," *J. Cardiovasc. Surg.* **53**(Suppl 1), 145–149 (2012).

50. I. A. Pestana et al., "Early experience with fluorescent angiography in free-tissue transfer reconstruction," *Plast. Reconstr. Surg.* **123**(4), 1239–1244 (2009).
51. D. P. Taggart et al., "Preliminary experience with a novel intraoperative fluorescence imaging technique to evaluate the patency of bypass grafts in total arterial revascularization," *Ann. Thorac. Surg.* **75**(3), 870–873 (2003).
52. P. H. Connolly et al., "Indocyanine green angiography aids in prediction of limb salvage in vascular trauma," *Ann. Vasc. Surg.* **29**(7), 1453.e1–1453.e4 (2015).
53. K. Igari et al., "Intraarterial injection of indocyanine green for evaluation of peripheral blood circulation in patients with peripheral arterial disease," *Ann. Vasc. Surg.* **28**(5), 1280–1285 (2014).
54. K. Igari et al., "Indocyanine green angiography for the diagnosis of peripheral arterial disease with isolated infrapopliteal lesions," *Ann. Vasc. Surg.* **28**(6), 1479–1484 (2014).
55. K. Igari et al., "Quantitative evaluation of microvascular dysfunction in peripheral neuropathy with diabetes by indocyanine green angiography," *Diabetes Res. Clin. Pract.* **104**(1), 121–125 (2014).
56. K. Igari et al., "Quantitative evaluation of the outcomes of revascularization procedures for peripheral arterial disease using indocyanine green angiography," *Eur. J. Vasc. Endovasc. Surg.* **46**(4), 460–465 (2013).
57. D. Perry et al., "Intraoperative fluorescence vascular angiography: during tibial bypass," *J. Diabetes Sci. Technol.* **6**(1), 204–208 (2012).
58. H. Mothes et al., "Indocyanine-green fluorescence video angiography used clinically to evaluate tissue perfusion in microsurgery," *J. Trauma.* **57**(5), 1018–1024 (2004).
59. J. D. Braun et al., "Early quantitative evaluation of indocyanine green angiography in patients with critical limb ischemia," *J. Vasc. Surg.* **57**(5), 1213–1218 (2013).
60. A. Zimmermann et al., "Early postoperative detection of tissue necrosis in amputation stumps with indocyanine green fluorescence angiography," *Vasc. Endovasc. Surg.* **44**(4), 269–273 (2010).
61. M. L. J. Landsman et al., "Light-absorbing properties, stability, and spectral stabilization of indocyanine green," *J. Appl. Physiol.* **40**, 575–583 (1976).
62. <http://www.drugs.com/support/about.html>.
63. M. W. Hope-Ross ICG dye: physical and pharmacological properties, in *Indocyanine Green Angiography*, L.A. Yannuzzi, R.W. Flower, and J.S. Slakter, Eds., pp. 46–49, Mosby-Year Book, St. Louis (1997).
64. M. S. Fineman et al., "Safety of indocyanine green angiography during pregnancy," *Arch. Ophthalmol.* **119**, 353–355 (2001).
65. B. F. Hochheimer, "Angiography of the retina with indocyanine green," *Arch. Ophthalmol.* **86**, 564–565 (1971).
66. J. Caesar et al., "The use of indocyanine green in the measurement of hepatic blood flow and as a test for hepatic function," *Clin. Sci.* **21**, 43–57 (1961).
67. C. A. Goresky, "Initial distribution and rate of uptake of sulfobromophthalein in the liver," *Am. J. Physiol.* **207**, 13–17 (1964).
68. C. M. Levy et al., "Physiology of dye extraction by the liver: comparative studies of sulfobromophthalein and indocyanine green," *Ann. N. Y. Acad. Sci.* **111**, 161–175 (1963).
69. D. Briers et al., "Laser speckle contrast imaging: theoretical and practical limitations," *J. Biomed. Opt.* **18**(6), 066018 (2013).
70. D. A. Boas and A. K. Dunn, "Laser speckle contrast imaging in biomedical optics," *J. Biomed. Opt.* **15**(1), 011109 (2010).
71. K. Basak, M. Manjunatha, and P. K. Dutta, "Review of laser speckle-based analysis in medical imaging," *Med. Biol. Eng. Comput.* **50**(6), 547–558 (2012).
72. M. Draijer et al., "Review of laser speckle contrast techniques for visualizing tissue perfusion," *Lasers Med. Sci.* **24**, 639–651 (2009).
73. J. Senarathna et al., "Laser speckle contrast imaging: theory, instrumentation and applications," *IEEE Rev. Biomed. Eng.* **6**, 99–110 (2013).
74. J. D. Briers and S. Webster, "Laser speckle contrast analysis (LASCA): a non-scanning full-field technique for monitoring capillary blood flow," *J. Biomed. Opt.* **1**, 174–179 (1996).
75. H. Cheng et al., "Modified laser speckle imaging method with improved spatial resolution," *J. Biomed. Opt.* **8**, 559–564 (2003).
76. Goodman, *Statistical Optics*, Wiley & Sons, New York (1985).
77. J. C. Ramirez-San-Juan et al., "Impact of velocity distribution assumption on simplified laser speckle imaging equation," *Opt. Express.* **16**(5), 3197–3203 (2008).
78. P. Miao et al., "Random process estimator for laser speckle imaging of cerebral blood flow," *Opt. Express* **18**(1), 218–236 (2010).
79. E. L. Towle et al., "Comparison of indocyanine green angiography and laser speckle contrast imaging for the assessment of vascular perfusion," *Neurosurgery* **71**(5), 1023–1031 (2012).
80. D. M. Burmeister et al., "Utility of spatial frequency domain imaging (SFDI) and laser speckle imaging (LSI) to non-invasively diagnose burn depth in a porcine model," *Burns* **41**(6), 1242–1252 (2015).
81. T. Furuta et al., "Free flap blood flow evaluated using two-dimensional laser speckle flowgraphy," *Int. J. Otolaryngol.* 297251 (2011).
82. *Optical Coherence Tomography: Technology and Applications*, J. G. Fujimoto and W. Drexler, Eds., Springer Berlin Heidelberg, New York (2008).
83. D. P. Popescu et al., "Optical coherence tomography: fundamental principles, instrumental designs and biomedical applications," *Biophys. Rev.* **3**(3), 155–169 (2011).
84. A. H. Zhou, "A survey of optical imaging techniques for assessing wound healing," *Int. J. Intell. Control Syst.* **17**(3), 79–85 (2012).
85. D. W. Paul et al., "Noninvasive imaging technologies for cutaneous wound assessment: a review," *Wound Repair Regen.* **23**(2), 149–162 (2015).
86. N. Ifimia et al., "Combined reflectance confocal microscopy/optical coherence tomography imaging for skin burn assessment," *Biomed. Opt. Express* **4**(5), 680–695 (2013).
87. J. Kim et al., "Optical coherence tomography speckle reduction by a partially spatially coherent source," *J. Biomed. Opt.* **10**(6), 064034 (2005).
88. D. P. Popescu, M. D. Hewko, and M. G. Sowa, "Speckle noise attenuation in optical coherence tomography by compounding images acquired at different positions of the sample," *Opt. Commun.* **269**(1), 247–251 (2007).
89. A. E. Desjardins et al., "Angle-resolved optical coherence tomography with sequential angular selectivity for speckle reduction," *Opt. Express* **15**, 6200–6209 (2007).
90. D. L. Marks, T. S. Ralston, and S. A. Boppart, "Speckle reduction by I-divergence regularization in optical coherence tomography," *J. Opt. Soc. Am. A* **22**(11), 2366–2371 (2005).
91. T. R. Hillman et al., "Correlation of static speckle with sample properties in optical coherence tomography," *Opt. Lett.* **31**(2), 190–192 (2006).
92. M. S. Mahmud et al., "Review of speckle and phase variance optical coherence tomography to visualize microvascular networks," *J. Biomed. Opt.* **18**(5), 050901 (2013).
93. G. J. Pettet et al., "A model of wound-healing angiogenesis in soft tissue," *Math. Biosci.* **136**, 35–63 (1995).
94. Y. M. Liew et al., "In vivo assessment of human burn scars through automated quantification of vascularity using optical coherence tomography," *J. Biomed. Opt.* **18**(6), 061213 (2013).
95. J. Enfield, E. Jonathan, and M. Leahy, "In vivo imaging of the microcirculation of the volar forearm using correlation mapping optical coherence tomography (cmOCT)," *Biomed. Opt. Express* **2**(5), 1184–1193 (2011).
96. G. J. Liu et al., "High-resolution imaging of microvasculature in human skin in-vivo with optical coherence tomography," *Opt. Express* **20**, 7694–7705 (2012).
97. Y. Zhao et al., "Phase-resolved optical coherence tomography and optical Doppler tomography for imaging blood flow in human skin with fast scanning speed and high velocity sensitivity," *Opt. Lett.* **25**, 114–116 (2000).
98. L. Conroy, R. S. DaCosta, and I. A. Vitkin, "Quantifying tissue microvasculature with speckle variance optical coherence tomography," *Opt. Lett.* **37**, 3180–3182 (2012).
99. H. M. Varma et al., "Speckle contrast optical coherence tomography: A new method for deep tissue three-dimensional tomography of blood flow," *Biomed. Opt. Express* **5**(4), 1275–1289 (2014).
100. L. An, J. Qin, and R. K. Wang, "Ultrahigh sensitive optical microangiography for in-vivo imaging of microcirculations within human skin tissue beds," *Opt. Express* **18**(8), 8220–8228 (2010).
101. G. Liu et al., "A comparison of Doppler optical coherence tomography methods," *Biomed. Opt. Express* **3**(10), 2669–2680 (2012).
102. J. Allen, "Photoplethysmography and its application in clinical physiological measurement," *Physiol. Meas.* **28**(3), R1 (2007).
103. A. Reisner et al., "Utility of the photoplethysmogram in circulatory monitoring," *Anesthesiology* **108**(5), 950–958 (2008).

104. M. E. Alnaeb et al., "Optical techniques in the assessment of peripheral arterial disease," *Curr. Vasc. Pharmacol.* **5**(1), 53–59 (2007).
105. J. Allen et al., "A prospective comparison of bilateral photoplethysmography versus ankle-brachial pressure index for detecting and quantifying lower limb peripheral arterial disease," *J. Vasc. Surg.* **47**, 794–802 (2008).
106. T. Yamada et al., "Clinical reliability and utility of skin perfusion pressure measurement in ischemic limbs—comparison with other noninvasive diagnostics methods," *J. Vasc. Surg.* **47**(2), 318–323 (2008).
107. P. B. Dattilo and I. P. Casserly, "Critical limb ischemia: endovascular strategies for limb salvage," *Prog. Cardiovas. Dis.* **54**(1), 47–60 (2011).
108. L. Caruana, C. Formosa, and K. Cassar, "Prediction of wound healing after minor amputations of the diabetic foot," *J. Diabetes Complications* **29**(6), 834–837 (2015).
109. C. Scanlon et al., "Interrater and intrarater reliability of photoplethysmography for measuring toe blood pressure and toe-brachial index in people with diabetes mellitus," *J. Foot Ankle Res.* **5**, 13 (2012).
110. M. Elgendi, "On the analysis of fingertip photoplethysmogram signals," *Curr. Cardio. Rev.* **8**, 14–25 (2012).
111. A. A. Kamshilin et al., "A new look at the essence of the imaging photoplethysmography," *Sci. Rep.* **5**, 10494 (2015).
112. T. Tamura et al., "Wearable photoplethysmographic sensors—past and present," *Electronics* **3**(2), 282–302 (2014).
113. G. Bal, "Inverse transport theory and applications," *Inverse Prob.* **25**, 053001 (2009).
114. A. D. Kim, "Transport theory for light propagation in biological tissue," *J. Opt. Soc. Am. A.* **21**(5), 820–827 (2004).
115. J. Schotland, "Direct reconstruction methods in optical tomography," *Lect. Notes Math.* **2035**, 1–23 (2012).
116. F. Martelli, "ABC of near infrared photon migration in tissues: the diffusive regime of propagation," *J. Near Infrared Spectrosc.* **20**(1), 29–42 (2012).
117. W. M. Star, "Diffusion theory of light transport," in *Optical-Thermal Response of Laser-Irradiated Tissue*, A. J. Welch and M. J. C. van Gemert, Eds., pp. 131–206, Plenum Press, New York (1995).
118. S. L. Jacques and B. W. Pogue, "Tutorial on diffuse light transport," *J. Biomed. Opt.* **13**(4), 041302 (2008).
119. L. Wang, S. L. Jacques, and L. Zheng, "MCML—Monte Carlo modeling of light transport in multi-layered tissues," *Comput. Methods Programs Biomed.* **47**, 131–146 (1995).
120. C. Zhu and Q. Liu, "Review of Monte Carlo modeling of light transport in tissues," *J. Biomed. Opt.* **18**(5), 050902 (2013).
121. W. J. Jeffcoate et al., "Use of HSI to measure oxygen saturation in the lower limb and its correlation with healing foot ulcers in diabetes," *Diabetic Med.* **32**, 798–802 (2015).
122. D. Yudovsky, A. Nouvong, and L. Pilon, "Hyperspectral imaging in diabetic foot wound care," *J. Diabetes Sci. Technol.* **4**(5), 1099–1113 (2010).
123. D. T. Ubbink and B. Koopman, "Near-infrared spectroscopy in the routine diagnostic work-up of patients with leg ischaemia," *Eur. J. Vasc. Endovasc. Surg.* **31**(4), 394–400 (2006).
124. M. Vardi and A. Nini, "Near-infrared spectroscopy for evaluation of peripheral vascular disease. A systematic review of literature," *Eur. J. Vasc. Endovasc. Surg.* **35**(1), 68–74 (2008).
125. F. Manfredini et al., "Near-infrared spectroscopy assessment following exercise training in patients with intermittent claudication and in untrained healthy participants," *Vasc. Endovascular Surg.* **46**(4), 315–324 (2012).
126. D. R. King et al., "Surgical wound debridement sequentially characterized in a porcine burn model with multispectral imaging," *Burns* **41**, 1478–1487 (2015).
127. M. A. Calin et al., "Characterization of burns using hyperspectral imaging technique—a preliminary study," *Burns* **41**, 118–124 (2015).
128. K. M. Cross et al., "Clinical utilization of near-infrared spectroscopy for burn depth assessment," *Wound Repair Regen.* **15**, 332–340 (2007).
129. M. G. Sowa et al., "Classification of burn injuries using near-infrared spectroscopy," *J. Biomed. Opt.* **11**(5), 054002 (2006).
130. S. Zhang et al., "Multimodal imaging of cutaneous wound tissue," *J. Biomed. Opt.* **20**(1), 016016 (2015).
131. A. Basiri et al., "Use of a multi-spectral camera in the characterization of skin wounds," *Opt. Express* **18**, 3244–3257 (2010).
132. M. G. Sowa et al., "The utility of near infrared imaging in intra-operative prediction of flap outcome: a reverse McFarlane skin flap model study," *J. Near Infrared Spectrosc.* **20**(5), 601–615 (2012).
133. M. F. Stranc et al., "Assessment of tissue viability using near infrared spectroscopy," *Br. J. Plast. Surg.* **51**, 210–217 (1998).
134. J. McKenna et al., "Assessing flap perfusion: optical spectroscopy vs venous doppler ultrasound," *J. Otolaryngol.-Head Neck Surg.* **38**(5), 587–594 (2009).
135. A. Kellar, "A new diagnostic algorithm for early prediction of vascular compromise in 208 microsurgical flaps using tissue oxygen saturation measurements," *Ann. Plast. Surg.* **62**, 538–543 (2009).
136. M. S. Chin et al., "Hyperspectral imaging as an early biomarker for radiation exposure and microcirculatory damage," *Front. Oncol.* **5**, 232 (2015).
137. M. R. Hee et al., "Polarization sensitive low coherence reflectometer for birefringence characterization and ranging," *J. Opt. Soc. Am. B.* **9**, 903–908 (1992).
138. D. Brett, "A review of collagen and collagen-based wound dressings," *Wounds* **20**(12), 347–356 (2008).
139. A. T. Yeh et al., "Imaging wound healing using optics coherence tomography and multiphoton microscopy in an in vitro skin-equivalent model," *J. Biomed. Opt.* **9**, 248–253 (2004).
140. J. T. Oh et al., "Quantification of the wound healing using polarization-sensitive optical coherence tomography," *J. Biomed. Opt.* **11**(4), 041124 (2006).
141. P. Gong et al., "Imaging of skin birefringence for human scar assessment using polarization-sensitive optical coherence tomography aided by vascular masking," *J. Biomed. Opt.* **19**(12), 126014 (2014).
142. S. J. Lin, S. H. Jee, and C. Y. Dong, "Multiphoton microscopy: a new paradigm in dermatological imaging," *Eur. J. Dermatol.* **17**, 361–366 (2007).
143. B. R. Masters, P. T. So, and E. Gratton, "Multiphoton excitation fluorescence microscopy and spectroscopy of in vivo human skin," *Biophys. J.* **72**, 2405–2412 (1997).
144. E. Yew, C. Rowlands, and P. T. So, "Application of multiphoton microscopy in dermatological studies: a mini-review," *J. Innovative Opt. Health Sci.* **7**(5), 1330010 (2014).
145. A. C. Chen et al., "Second harmonic generation and multiphoton microscopic detection of collagen without the need for species specific antibodies," *Burns* **37**(6), 1001–1009 (2011).
146. W. R. Zipfel, R. M. Williams, and W. W. Webb, "Nonlinear magic: multiphoton microscopy in the biosciences," *Nat. Biotechnol.* **21**, 1369–1377 (2003).
147. W. R. Zipfel et al., "Live tissue intrinsic emission microscopy using multiphoton-excited native fluorescence and second harmonic generation," *Proc. Nat. Acad. Sci. U. S. A.* **100**(12), 7075–7080 (2003).
148. P. J. Campagnola et al., "Three-dimensional high-resolution second-harmonic generation imaging of endogenous structural proteins in biological tissues," *Biophys. J.* **82**(1), 493–508 (2002).
149. G. Cox et al., "Resolution of second harmonic generation microscopy," *Proc. 15th Int. Cong. Electron Microsc.*, Durban, South Africa, Vol. 2, pp. 331–332, (2002).
150. F. A. Navarro et al., "Two photon confocal microscopy in wound healing," *Proc. SPIE* **4262**, 27–40 (2001).
151. T. Luo et al., "Visualization of collagen regeneration in mouse dorsal skin using second harmonic generation microscopy," *Laser Phys.* **19**, 478–482 (2009).
152. M. B. Brewer et al., "Multiphoton imaging of excised normal skin and keloid scar: Preliminary investigations," *Proc. SPIE* **5312**, 204–208 (2004).
153. A. Meshkinpour et al., "Treatment of hypertrophic scars and keloids with a radiofrequency device: a study of collagen effects," *Lasers Surg. Med.* **37**, 343–349 (2005).
154. G. Chen et al., "Nonlinear spectral imaging of human hypertrophic scar based on two-photon excited fluorescence and second-harmonic generation," *Br. J. Dermatol.* **161**(1), 48–55 (2009).
155. V. Da Costa et al., "Nondestructive imaging of live human keloid and facial tissue using multiphoton microscopy," *Arch. Facial Plast. Surg.* **10**, 38–43 (2008).

156. S. Chen et al., "Differentiating keloids from normal and hypertrophic scar based on multiphoton microscopy," *Laser Phys.* **20**(4), 900–903 (2010).
157. X. Zhu et al., "Marginal characteristics of skin scarred dermis quantitatively extracted from multiphoton microscopic imaging," *Proc. SPIE* **7845**, 784528 (2010).
158. J. Chen et al., "Multiphoton microscopy study of the morphological and quantity changes of collagen and elastic fiber components in keloid disease," *J. Biomed. Opt.* **16**, 051305 (2011).
159. L. B. Mostaço-Guidolin et al., "Collagen morphology and texture analysis: from statistics to classification," *Sci. Rep.* **3**, 2190 (2013).
160. L. B. Mostaço-Guidolin et al., "Evaluation of texture parameters for the quantitative description of multimodal nonlinear optical images from atherosclerotic rabbit arteries," *Phys. Med. Biol.* **56**(16), 5319–5334 (2011).
161. Y. Liu et al., "Texture analysis of collagen second-harmonic generation images based on local difference local binary pattern and wavelets differentiates human skin abnormal scars from normal scars," *J. Biomed. Opt.* **20**(1), 016021 (2015).
162. R. Cicchi et al., "Scoring of collagen organization in healthy and diseased human dermis by multiphoton microscopy," *J. Biophotonics* **3**(1–2), 34–43 (2010).
163. X. Zhu et al., "Quantification of scar margin in keloid different from atrophic scar by multiphoton microscopic imaging," *Scanning* **33**, 195–200 (2011).
164. K. Koenig et al., "Clinical two-photon microendoscopy," *Microsc. Res. Tech.* **70**, 398–402 (2007).
165. K. Koenig, "Hybrid multiphoton multimodal tomography of in vivo human skin," *IntraVital* **1**(1), 11–26 (2012).
166. K. König, "Clinical multiphoton tomography," *J. Biophotonics* **1**(1), 13–23 (2008).
167. M. Weinigel et al., "Compact clinical high-NA multiphoton endoscopy," *Proc. SPIE* **8217**, 821706 (2012).

Biographies for the authors are not available.